THE UNIVERSITY OF

ARIZONA

TUCSON ARIZONA

March 1994

FINAL REPORT

NASA-Langley Contract Number 1-1422

NAG1-1433

Numerical Simulation of Receptivity and Transition in a Boundary Layer on a Flat Plate with a Suction Hole

NASA Project Monitor: Dr. Ronald D. Joslin

Principal Investigator: Dr. Hermann F. Fasel

Department of Aerospace and Mechanical Engineering

The University of Arizona

Tucson, Arizona 85721

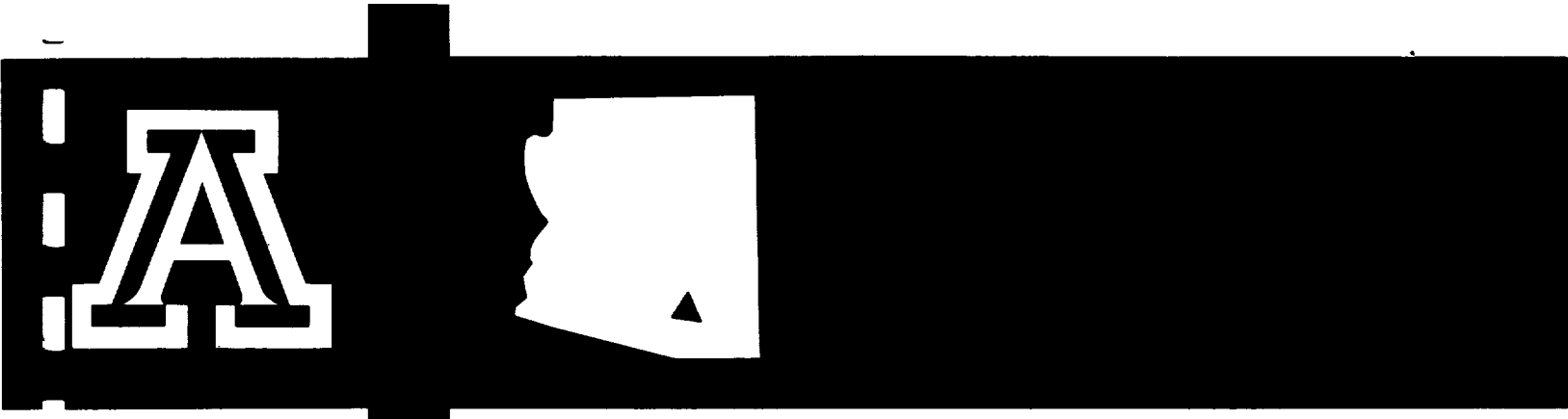

ENGINEERING EXPERIMENT STATION
COLLEGE OF ENGINEERING AND MINES
THE UNIVERSITY OF ARIZONA
TUCSON, ARIZONA 85721

1. Update of Numerical Method

Since our last progress report (September 1993) we have modified our Navier-Stokes solver to allow for unsteady boundary conditions to be imposed at the inflow boundary. Because the streamwise derivatives are discretized with 3-point compact differences, there is no need for special treatment of the points adjacent to the inflow boundary, provided that all necessary derivatives are properly specified at the boundary points. The unsteady boundary conditions can be obtained from a previous computation, from a solution of the parabolized stability equations (PSE), or from an analytical exact or approximate solution of the Navier-Stokes equations (e.g. an asymptotic expansion solution to model a sound wave interacting with the boundary layer).

2. Numerical Simulation of the Northrop Suction Experiments

2.1 Overview

We have perfomed a more detailed analysis of our numerical simulations of the Northrop suction experiments (Goldsmith, 1957). In these experiments Goldsmith studied the flow inside the entrance region of a circular pipe. The experimental parameters were chosen such that the flow was mostly irrotational, with a thin boundary layer developing along the wall. Suction was applied through one row of holes along the circumference of the pipe (Fig.1). Goldsmith found that the effects of the suction on the boundary layer inside the pipe could be described by two nondimensional parameters, a nondimensional wall shear

$$T = \frac{s^2}{2\nu}\left(\frac{\partial u_B}{\partial y}\right)_{wall}\left(\frac{s-d}{s}\right)^{1.18} \tag{1}$$

and a nondimensional suction flux

$$F = \frac{1}{\nu}\frac{\Delta Q}{\Delta z}\left(\frac{s-d}{s}\right)^{0.62} \quad . \tag{2}$$

where

$\left(\frac{\partial u_B}{\partial y}\right)_{wall}$ wall vorticity of the unperturbed basic flow (without suction)

ν dynamic viscosity

$\Delta Q/\Delta z$ suction flow volume per unit length in azimuthal direction

s hole spacing

d hole diameter

For a given geometry and base flow, T is constant and F varies linearly with increasing suction strength.

For these two parameters he found a "critical suction curve". A part of this curve is shown in Fig.2, with F on the abscissa and T on the ordinate axis. For values of the parameters

T, F to the left of the critical suction curve, Goldsmith found stable vortices emerging from the holes and extending downstream in x-direction. For values T, F in between the two branches of the curve, he found vortex shedding and transition to turbulence. For values T, F to the right of the suction curve, he again found stable vortices, which, however, were aligned in the azimuthal direction.

A major finding of the experiments was that the critical suction curve is independent of the precise shape of the boundary layer profile, because only the wall vorticity appears in T. This allowed us to substitute a flat plate boundary layer in the numerical simulation for a pipe entrance boundary layer in the experiment, quasi "unrolling" the pipe onto a plate. To account for the finite circumference of the pipe, we imposed periodicity in the spanwise direction z (corresponding to the azimuthal direction θ in the experiments). In addition we imposed symmetry of the flow with respect to the $z = 0$ plane to reduce the memory and CPU-time requirements of the simulation.

The computational box is shown in Fig.4. In streamwise direction x the integration domain was 68 hole diameters long and was discretized with 961 gridpoints. In wall-normal direction y it extended to two boundary layer thicknesses and was discretized with 100 gridpoints. In spanwise dircetion we used 11 Fourier modes and 17 collocation points.

In the simulation, for the viscosity ν, freestream velocity U_∞, hole spacing s, hole diameter d and suction flow Q we chose the same values as in the experiment. The wall vorticity was matched by adjusting the distance between the suction holes and the leading edge. The suction velocity v was imposed as a boundary condition over the hole diameter d: $v(r) = v_0 \cos(\pi r/d)$ as shown in Fig.3.

The parameters F, T of the three numerical calculations we performed are marked in Fig.2. In all three calculations, the nondimensional wall shear was $T = 404$, this corresponds to a Reynolds number based on displacement thickness of $Re_\delta = 1224$ at the holes.

The corresponding numerical parameters for the simulations were: Freestream velocity $U_\infty = 15$ m/s, viscosity $\nu = 15 \times 10^{-6}$ m^2/s, hole spacing $s = 2.007362$ mm, hole diameter $d = 1.0287$ mm, distance from leading edge to hole centers $x_c = 0.50625$ m. In the calculation C1 (subcritical case) the nondimensional suction flux was $F = 35$, corresponding to a point in the stable region to the left of the critical suction curve. In the calculation C2 (weakly supercritical case) the nondimensional suction flux was $F = 46$. This point lies just inside the unstable region of the parameter space. It should be noted that there is considerable scatter of the original experimental data in this region. In the calculation C3 (strongly supercritical case) the nondimensional suction flux was $F = 58$, which is well inside the unstable region.

2.2 Subcritical Case C1

For this simulation, trailing vortices emerged from the holes as expected and extended downstream. Once the vortices had reached the outflow boundary, the flow field attained a steady state.

A three-dimensional contour plot of the magnitude of the streamwise vorticity $|\omega_x|$ is shown in Fig.5, with all lengths given in mm. Within the limits of the 3-D perspective, the region shown is drawn to scale in x, y, z. It extends from the centerplane of one suction hole at $z = 0$ to the centerplane of the adjacent suction hole to the right at $z = s$. In streamwise direction x, it extends approximately 1.5 hole diameters upstream of the hole centers and

approximately 6 hole diameters downstream. In wall normal direction, the region extends to approximately one half boundary layer thickness.

Between the vortices is a small recirculation region (see Fig.6) which extends about three hole diameters downstream of the holes.

From Fig.5 one can observe that vortices from adjacent holes are closer to each other than vortices from the same hole, as shown schematically in Fig.7. Consequently, the main interaction between those vortices causes a mutual uplifting, i.e. as the vortices extend in downstream direction they move away from the wall. Figs.9, 10, 11 show contours of the streamwise vorticity in the plane $z = s/3$. These plots essentially represent a cut through a vortex core. Superimposed on the vorticity contours are the velocity vectors (u, v) of the undisturbed boundary layer flow. Near the hole, the vortices are still close to the wall, where the slope of the (undisturbed) boundary layer is fairly constant. Thus as the vortices are lifted up, they move into a fluid layer with increased mean streamwise velocity. This leads to vortex stretching, which results in an increase of vorticity in downstream direction. Further downstream, as the vortices approach the edge of the boundary layer, the mean streamwise velocity no longer increases in vertical direction, and the growth of vorticity levels off.

In Fig.8, the streamwise vorticity ω_x at the vortex core is plotted versus the downstream distance x. At the holes, the vorticity attains a maximum and then falls of rapidly over a distance of three hole diameters. This distance is the same as the extent of the recirculation region mentioned above. From there on, the vorticity increases again, and grows approximately $\propto \sqrt{x}$. After 18 hole diameters, the vortex has risen to the edge of the boundary layer, and the growth becomes weaker.

2.3 Weakly Supercritical Case C2

In this case the flow field near the holes is qualitatively not very different from the previous case, as shown in Figs. 12 and 13. Two vortices emerge from each hole, and initially they appear steady. However, after 20 hole diameters downstream one can observe small fluctuations in the form of a periodic (both in space and time) thickening-thinning of the vortices. This is shown in Figs. 14 and 15, and it is reminiscent of the sinuous mode disturbances that are observed in vortex instabilities. Finally after 30 hole diameters the vortices break up (see Figs. 16 and 17). A Fourier analysis of the fluctuations shows a distinct peak at 1714 Hz. In the usual nondimensional unit for stability investigations $F=2\pi f\nu/{U_\infty}^2 \times 10^4$, this corresponds to F=7.18. This is much higher than any frequency in the amplified TS-band for the Blasius boundary layer.

For further analysis, the phase of the ω_x Fourier mode corresponding to 1714 Hz was calculated near the y, z location of the vortex core. In Fig.18, this phase is plotted versus downstream distance $x - x_c$. The phase is fairly constant over the first 15 diameters downstream of the hole. From there on it exhibits the typical pattern of a traveling wave, with the phase increasing by 2π over every wavelength. From the slope of the phase curve one can compute the phasespeed of the fluctuations, which is about 45 % of the freestream speed.

In Fig.19, the corresponding Fourier amplitude is plotted. After about 15 diameters downstream of the hole the amplitude begins to grow; this correlates with the change of the phase pattern in the previous figure.

2.4 Strongly Supercritical Case C3

In the third case C3, the flow is qualitatively very different from the first two cases. The fluctuations are strong already at the suction holes, and it appears that there is vortex shedding. This can be seen from the 3-D contour plots of the magnitude of the streamwise vorticity (Fig.20) and of the magnitude of the total vorticity (Fig.20).

Fig.22 shows timesignals of the spanwise vorticity at several downstream locations x, with $y, z = constant$. Near the hole the periodicity of the vortex shedding is clearly discernible in the curves. Further downstream the timesignal resembles more and more that of a turbulent flow.

Again we performed a Fourier analysis of the fluctuations. The frequency of the vortex shedding is approximately 735 Hz, which is much lower than the peak frequency in case C2. This correlates with Goldsmith's observation that the shedding frequency decreases with increasing suction strength. In Fig.23, the phase of the ω_z component of the 735 Hz fluctuation is plotted versus x. Contrary to the case C2, the phase exhibits a traveling wave pattern starting right at the holes. The phase speed, inferred from the slope, is about 45 % of the freestream speed.

2.5 Discussion

The computational results are in good qualitative (for lack of quantitative data) agreement with the experimental results. Our calculations confirmed the location of the lower branch of the critical suction curve, and its universal character (i.e. the curve is applicable to both to pipe flow boundary layers and flat plate boundary layers.).

Of particular interest are the results of calculation C2, the weakly supercritical case. From the experimental data it was not quite clear how the transition from the stable to the unstable region in parameter space takes place. In principle, it could be either due to vortex instability, or due to an instability of the recirculation region that forms between the vortices. Goldsmith attributed the observed turbulence to vortex shedding from the hole, which sets in once the suction strength is above the critical threshold. In contrast, our calculations indicate that (at least in some region of the parameter space F, T) the transition is caused by a vortex instability.

As the suction strength is further increased, we expect the onset of instability growth in the vortices to move upstream and eventually to coalesce with the recirculation region, leading to the vortex shedding observed in the experiments (and in calculation C3).

A major difference between the pipe-entrance boundary layer and the flat plate boundary layer is that the former is much more stable (in fact a useful neutral stability curve has yet to be established for this flow). Indeed, Goldsmith did not observe transition in the absence of suction. In contrast, with the parameters used in the simulations the Blasius boundary layer is unstable to small disturbances. We would expect transition to turbulence to occur sufficiently far downstream, even with the lowest suction strength (case C1). In view of this, the critical suction curve assumes a different character for the flat plate boundary layer: It separates regions where transition is guaranteed to occur due to suction effects alone (vz. in between the two branches) from those where transition may be caused by other effects.

3. Effect of suction holes in Laminar Flow Control

The motivation for using suction holes in laminar flow control is to change the stability characteristic of the boundary layer through wall suction. Suction through holes, however, can have undesired side effects: The holes may enhance receptivity to freestream disturbances, and they may generate crossflow in the boundary layer which can actually enhance transition, either directly through the suction or indirectly through the generation of streamwise vortices (see previous discussion).

In many LFC experiments, perforated panels are used to apply suction. Typical hole diameters are a fraction of a Tollmien-Schlichting wavelength $d = 1/5 \ldots 1/20\lambda_{TS}$, and the suction velocity are very small, on the order of 1 % of U_∞ (Harris et. al., 1992). However, the hole spacing (both in streamwise and spanwise direction) can be on the order of a TS-wavelength, and this may lead to resonance effects.

In our first numerical simulation of a suction-hole configuration that is relevant for LFC, we investigated the effect of a single spanwise row of suction holes ($d = 1/20\lambda_{TS}$) on both the steady boundary layer and on an oncoming TS-wave. However, to limit the CPU and memory requirements, we chose a hole spacing $s/d = 2$, which is somewhat denser than in practical applications.

The Reynoldsnumber at the x-location of the holes was $R_\delta = 1200$. The hole diameter d was 4/5 of the local displacement thickness δ, and the suction velocity averaged over one hole was 0.2 % of U_∞. Fig.24 shows a carpet plot of the mean 2-D streamwise velocity u that is induced by the holes, i.e. the change from the undisturbed Blasius boundary layer profile. The suction increases the u velocity near the wall by 0.08 % of U_∞, and there is a slight kink in the velocity profile directly above the holes. The first spanwise Fourier mode is plotted in Fig.25. Directly above the suction hole there is a peak of 0.37 % of U_∞, but downstream of the hole the velocity falls off rapidly. All higher spanwise modes are much smaller and also decay in x direction. Thus, the holes in this case are sufficiently small to avoid the generation of growing streamwise vortices. We also introduced a 2-D disturbance wave of nondimensional frequency F=1 and amplitude 10^{-6} at the inflow boundary. At the local Reynolds number this disturbance is weakly amplified in a Blasius boundary layer. After the flow had reached a periodic state, we performed a Fourier-analysis in time. Fig.26 shows the amplitudes of the u-velocity component of the 2-D TS waves: They are almost identical to those obtained for the case without suction, Close inspection reveals a small deviation near the wall directly above the suction hole. The amplitudes of the higher harmonics of the 2-D TS-wave are negligibly small. The amplitudes of any 3-D fluctuations are also negligibly small, and they decay away from the hole.

Next we calculated a case with a large hole diameter (4.8 local displacement thicknesses), and with a larger hole spacing of $s/d = 5$. The average suction velocity was again 0.2 % of U_∞. Fig.27 shows a carpet plot of the change of the mean 2-D streamwise velocity u that is induced by the holes. The larger holes cause a stronger initial adjustment of the boundary layer. However, the velocity drops off downstream of the holes, and the long-range effects of the larger holes on the mean 2-D flow are not much different from the small ones in the previous case.

The picture is quite different for the first spanwise Fourier mode, plotted in Fig.28. While the maximum of the u velocity above the holes is not much higher than in the previous case

(approx. 0.6 % of U_∞), at first it decays only very little downstream of the holes. Then, in contrast to before, the velocity increases again further downstream of the holes. This is a clear indication of the formation of streamwise vortices. Investigations of the effect of these vortices on TS-waves are currently under way.

4. Future Work

Due to the complexity of the research project and the many issues involved, we plan to proceed in three discrete steps in the next year.

1. We will continue the investigation of the short scale effects of a single row of suction holes on TS-waves. The important issues here are the scattering of TS-waves by the holes and resonances of certain spanwise modes due to the hole spacing. We also plan to examine the receptivity of the holes to freestream disturbances. There has been previous research in this area by means of asymptotic theory (Choudhari and Kerschen, 1990), albeit in a parameter range that is outside the scope of the present investigations (The characteristic streamwise lengthscales in Triple-Deck theory are of $\mathcal{O}(\lambda_{TS})$, whereas we consider holes which are very much smaller than λ_{TS}.). These results can provide a further reference for validation of our calculations.

2. Next we plan to extend our investigations to the generation of streamwise vortices by the holes, and to their effects on transition. It is known that even vanishingly weak streamwise vortices can have a strong effect on transition, but to date there are no quantitative predictions.

3. Finally, we will study the effects of an array of suction holes, consisting of several rows of holes in spanwise direction, aligned and/or staggered in streamwise direction. Here the questions are whether the downstream rows will increase or attenuate negative effects of the rows upstream (vz. vortices), and whether the streamwise spacing of the holes can cause resonances with disturbance waves.

References

Choudhari, M., Kerschen, E.J., 1990, "Instability wave patterns generated by interation of sound waves with three-dimensional wall suction or roughness," AIAA Paper 90-0119.

Goldsmith, J., 1957, "Critical Laminar Suction Parameters for Suction into an Isolated Hole or a Single Row of Holes," Northrop Aircraft Report No. BLC-95.

Harris, C. D., Brooks, C. W., Clukey, P. G., Stack, J. P., 1992, "The NASA Langley Laminar-Flow-Control Experiment on a Swept, Supercritical Airfoil," NASA Technical Memorandum 4309. 92N 22196

Figures

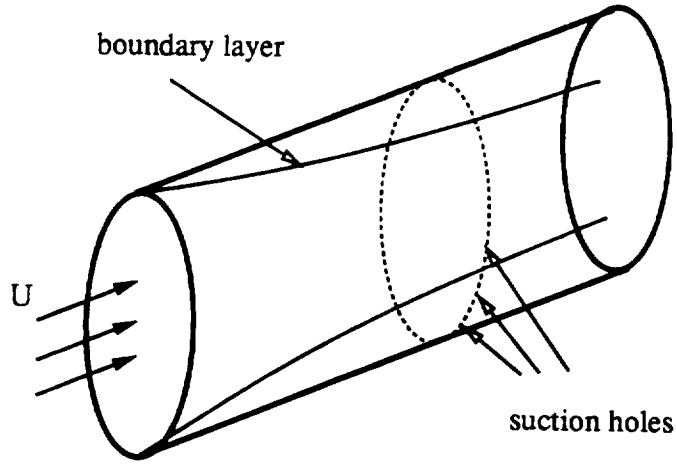

Figure 1: Schematic of Goldsmith's experiment: Flow in the entrance region of a pipe, with boundary layer suction through a row of holes along the circumference.

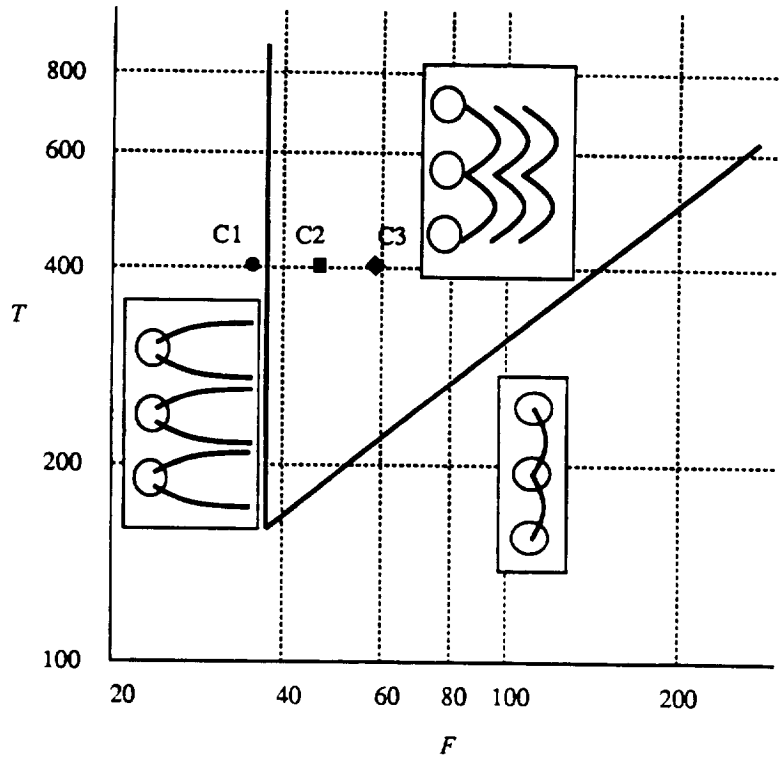

Figure 2: Critical Suction Curve. F is the nondimensional suction flux, T is the nondimensional wall shear. C1,C2,C3 are numerical computations. Indicated are regions of stable streamwise vortices, instability (vortex shedding), and stable spanwise vortices.

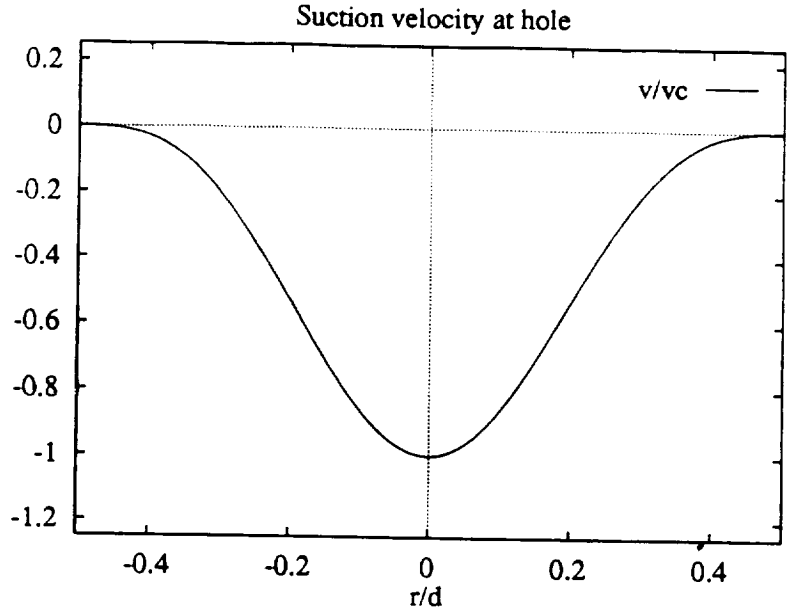

Figure 3: Suction velocity over one hole.

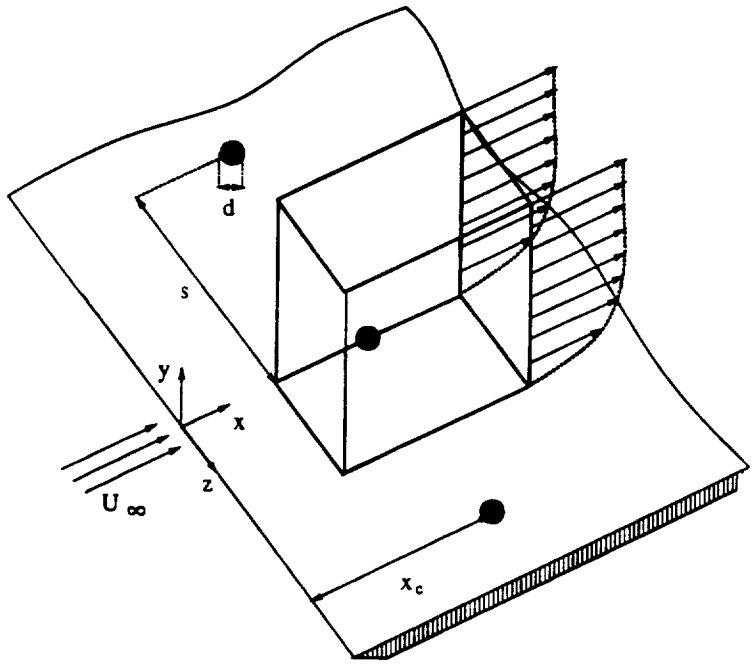

Figure 4: Schematic of integration domain.

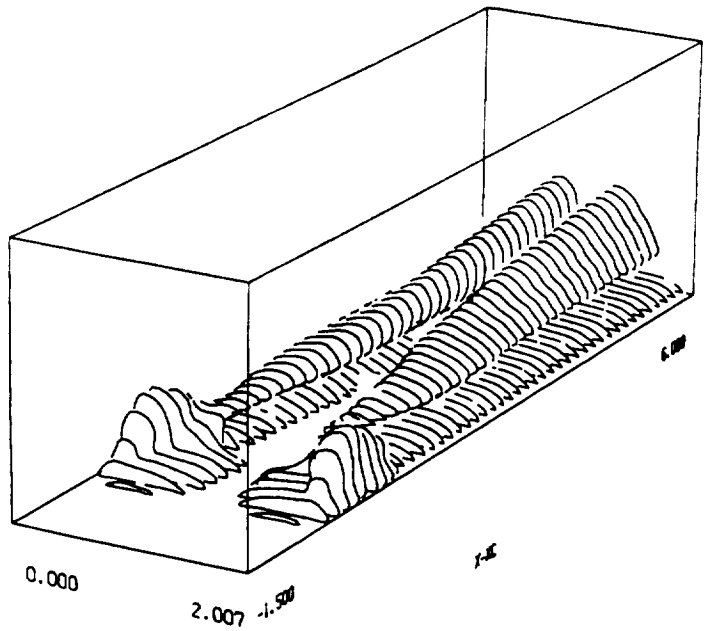

Figure 5: Case C1: Contourlines of $|\omega_x| = 30$, view from upstream.

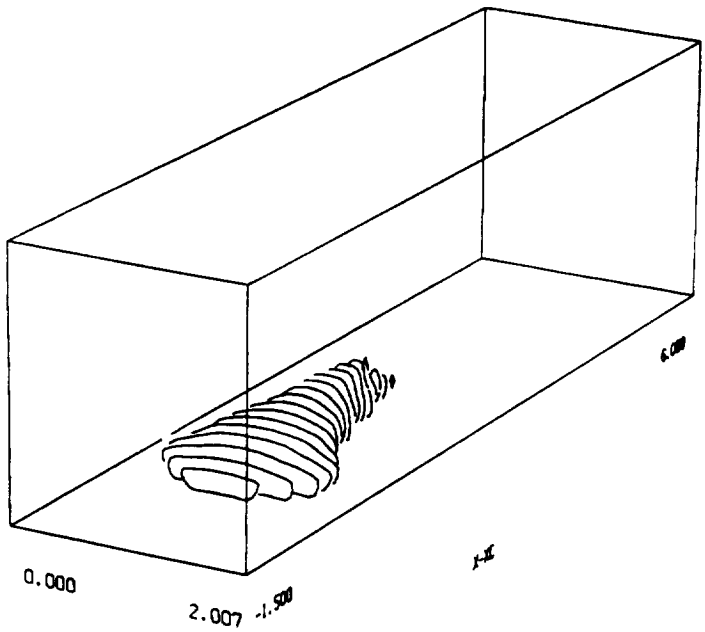

Figure 6: Case C1: Contourlines of $u = 0$, view from downstream.

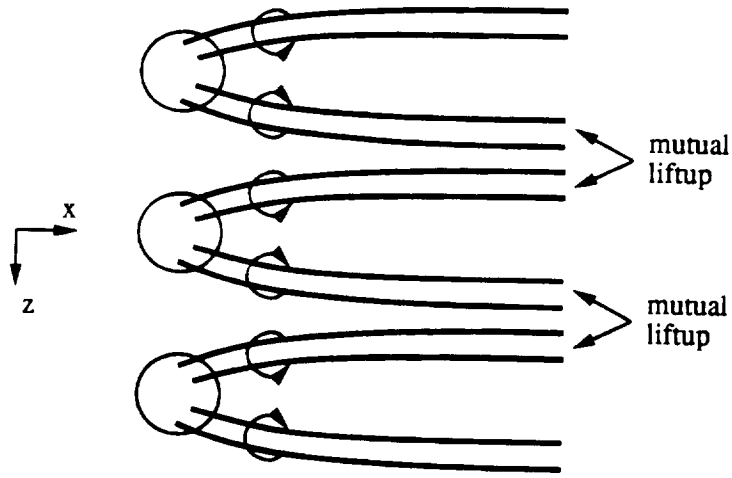

Figure 7: Schematic of holes with trailing vortices, view from top.

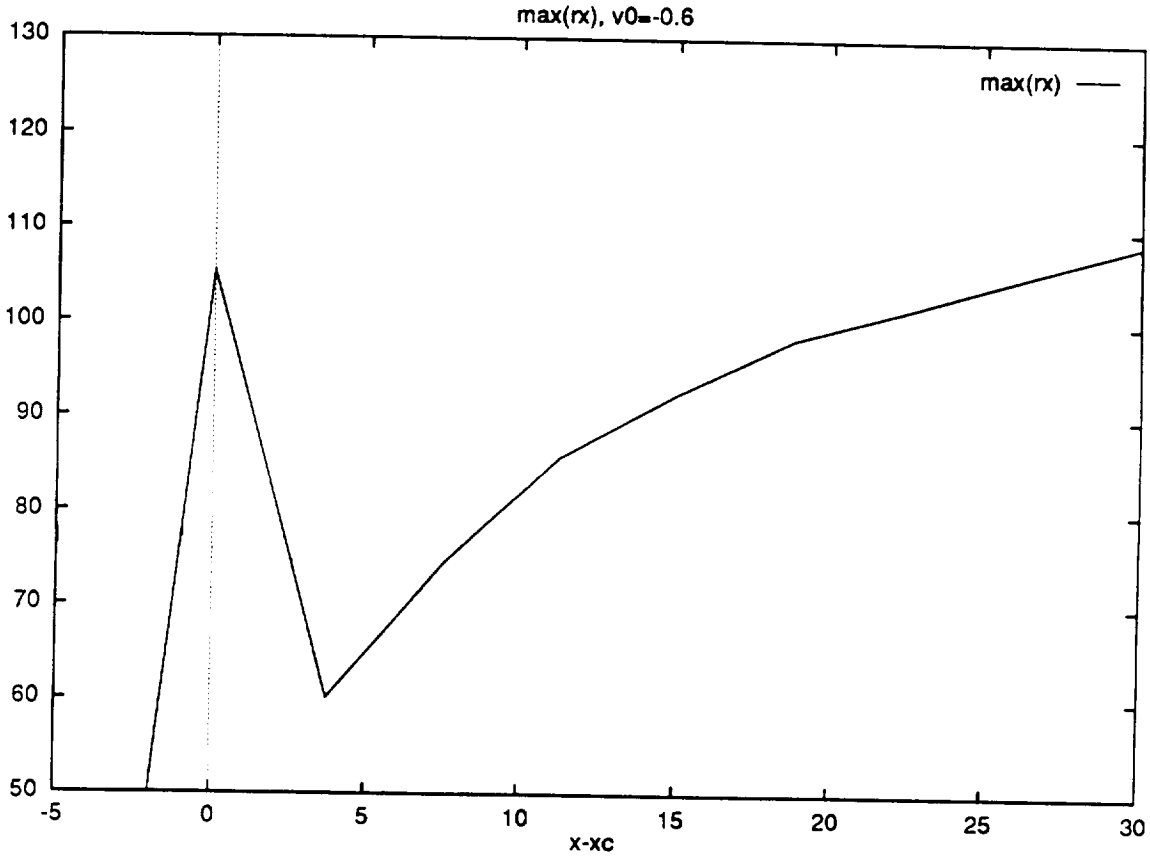

Figure 8: Case C1: Streamwise vorticity at vortex core, plotted over downstream distance $x - x_c$ (in mm).

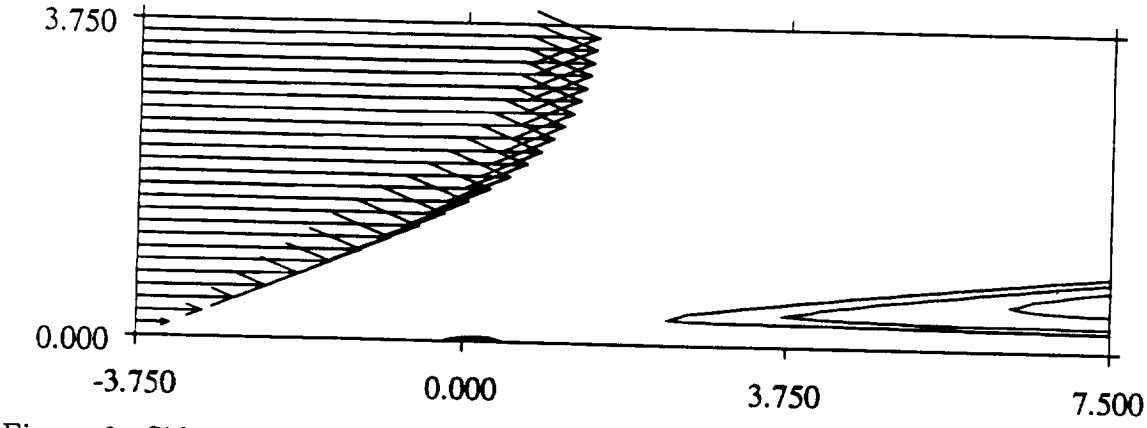

Figure 9: Sideview of vortices. Contours are levels of streamwise vorticity ω_x, arrows are velocity vectors of undisturbed boundary layer flow at left edge of plot. Drawn to scale in x, y (in mm); $x - x_c$ is distance from center of holes.

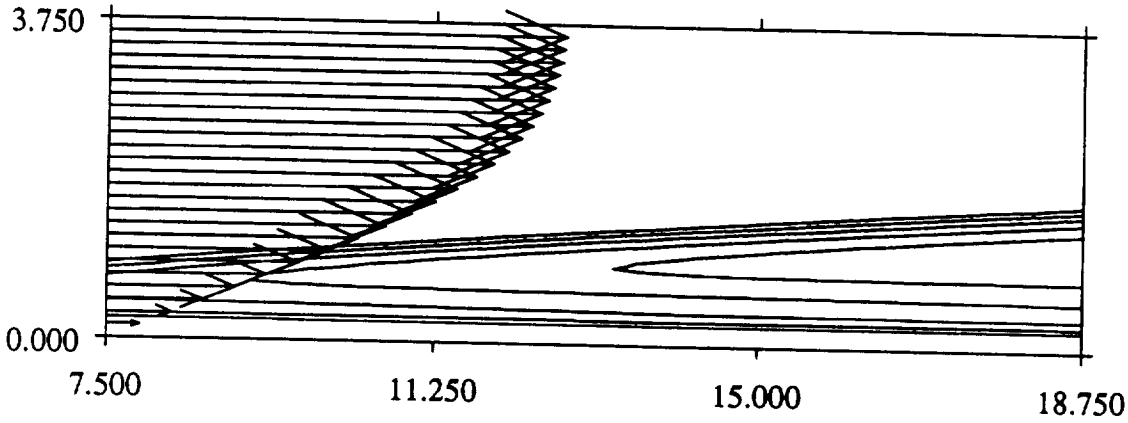

Figure 10: contd.

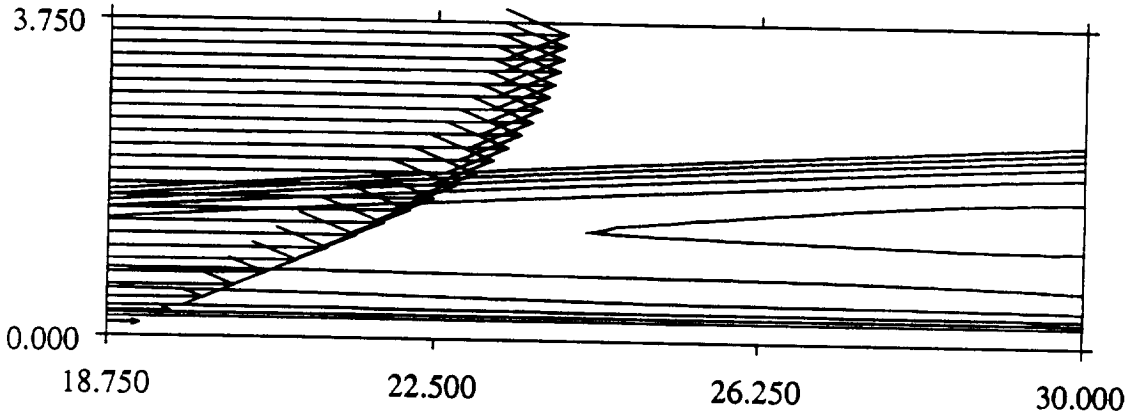

Figure 11: contd.

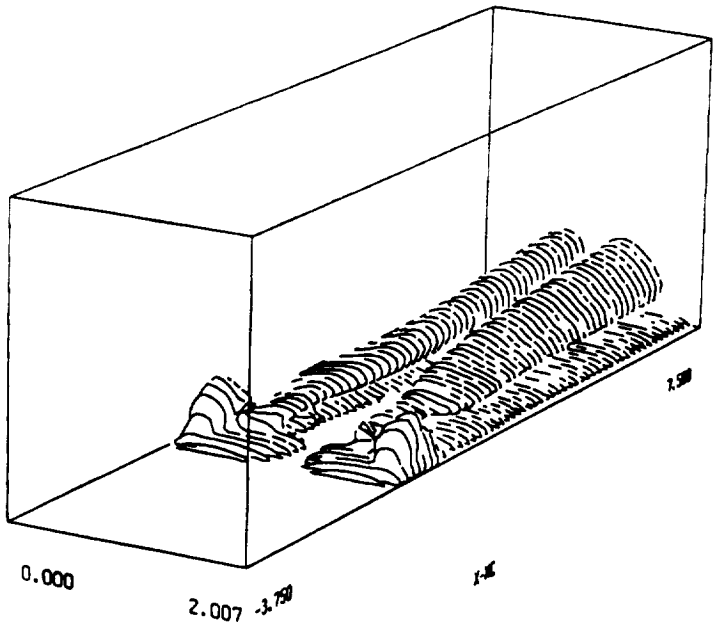

Figure 12: Case C2: Contours of $|\omega_x| = 30$, $x - x_c = -3.75 \ldots 7.5$.

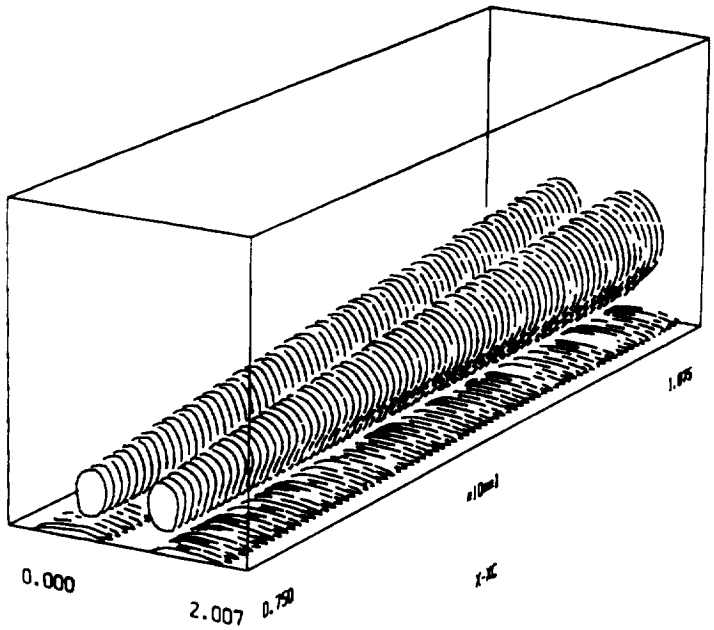

Figure 13: Case C2: Contours of $|\omega_x| = 60$, $x - x_c = 7.5 \ldots 18.25$.

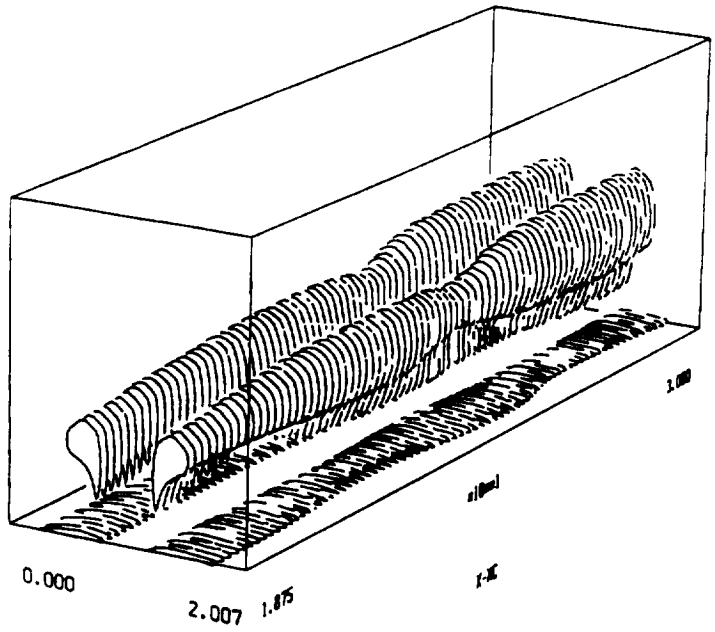

Figure 14: Case C2: Instantaneous contours of $|\omega_x| = 90$, $x - x_c = 18.25 \ldots 30.00$.

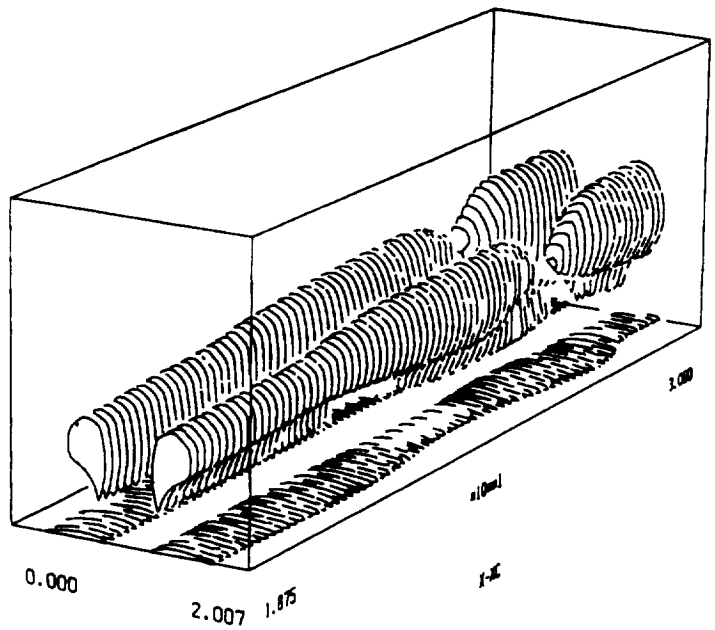

Figure 15: Case C2: Instantaneous contours of $|\omega_x| = 90$, $x - x_c = 18.25 \ldots 30.00$ at a later time.

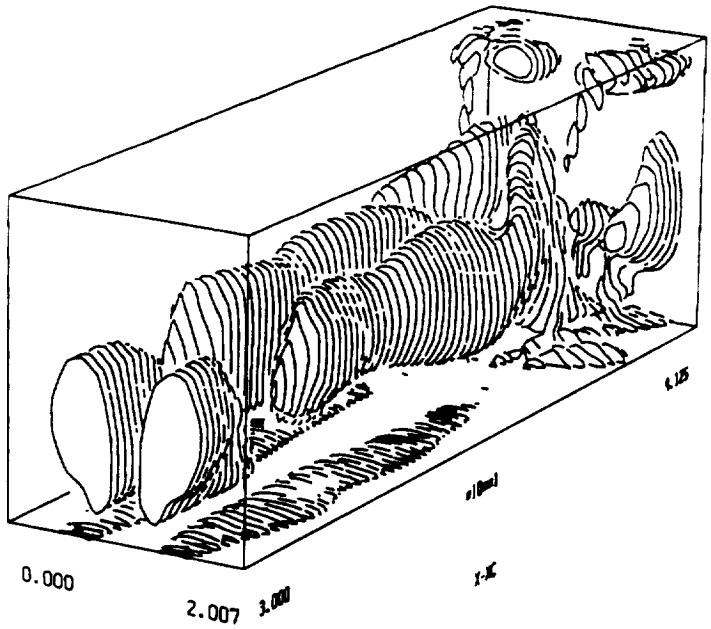

Figure 16: Case C2: Instantaneous contours of $|\omega_x| = 90$, $x - x_c = 30.00 \ldots 41.25$.

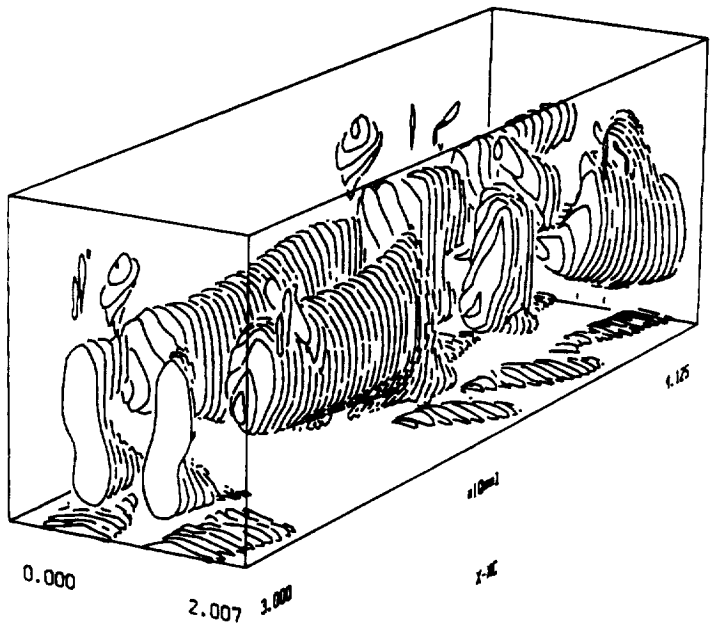

Figure 17: Case C2: Instantaneous contours of $|\omega_x| = 90$, $x - x_c = 30.00 \ldots 41.25$ at a later time.

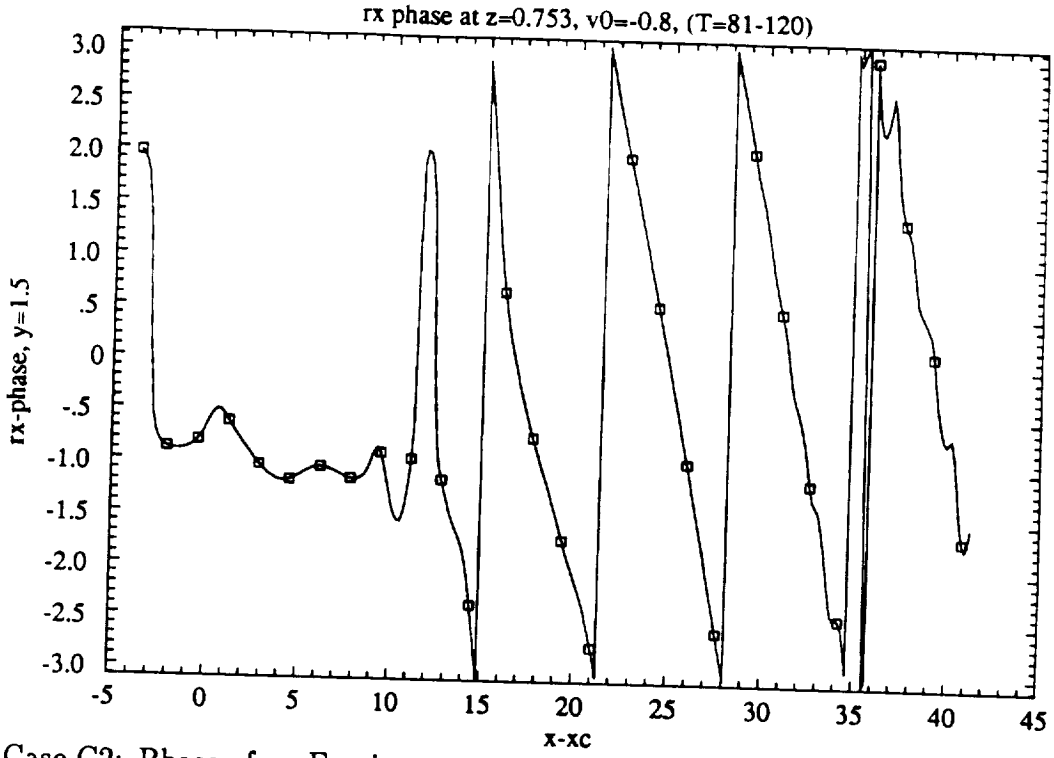

Figure 18: Case C2: Phase of ω_x Fourier component with frequency 1714 Hz, plotted versus x at constant $y = 1.5, , z = 0.753$

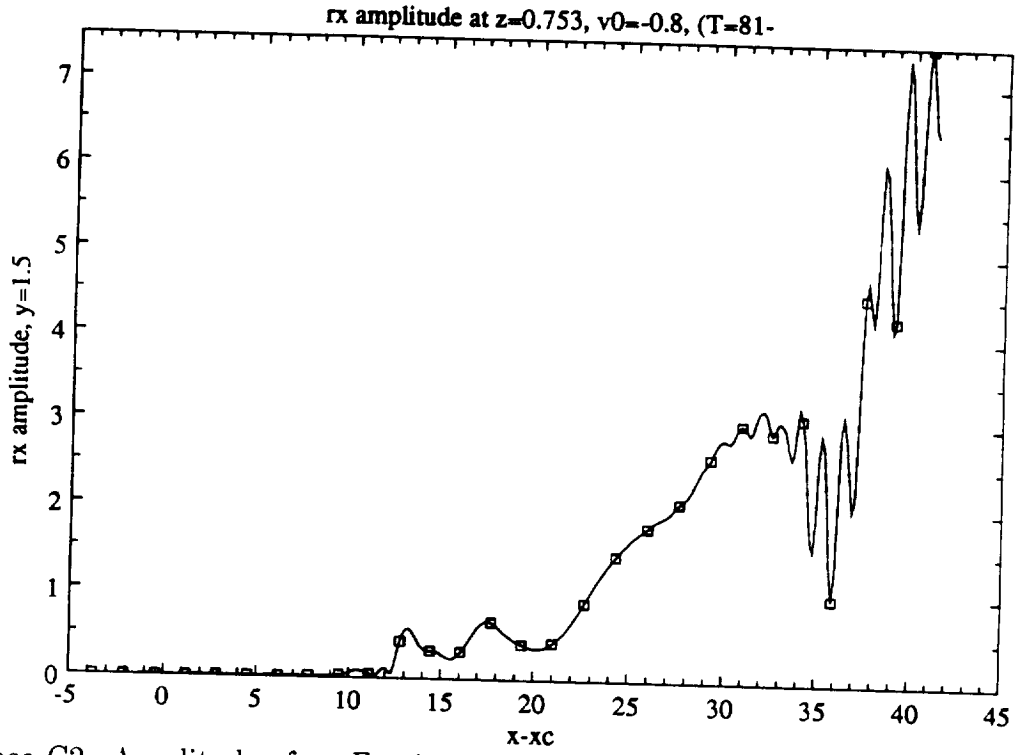

Figure 19: Case C2: Amplitude of ω_x Fourier component with frequency 1714 Hz, plotted versus x at constant $y = 1.5, , z = 0.753$

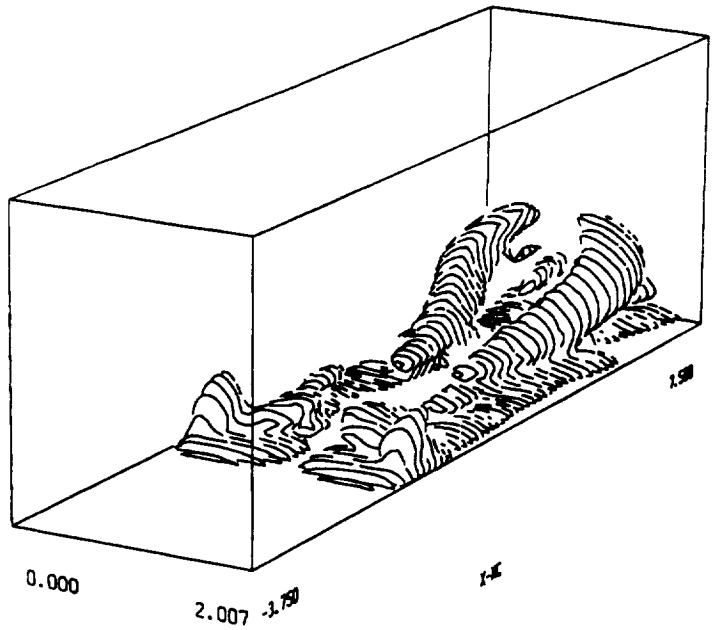

Figure 20: Case C3: Instantaneous contours of $|\omega_x| = 40$, $x - x_c = -3.75 \ldots 7.5$.

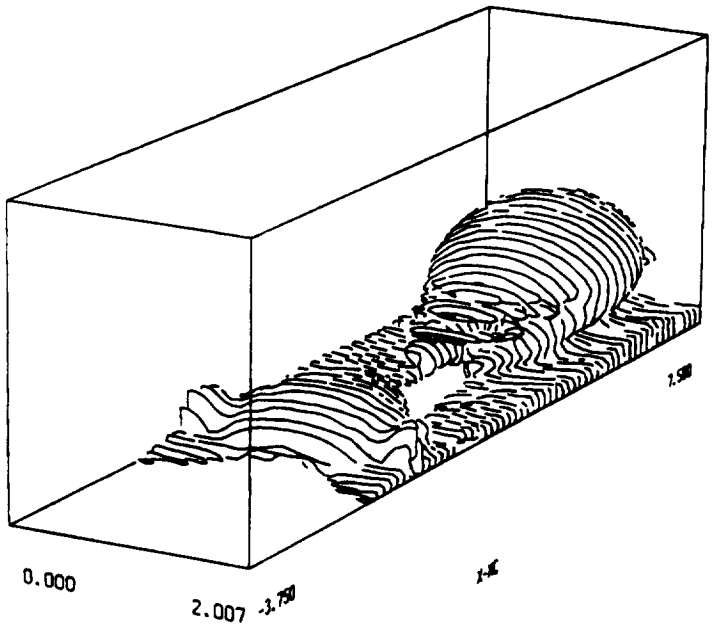

Figure 21: Case C2: Instantaneous contours of $|\omega| = 90$, $x - x_c = 7.5 \ldots 18.25$.

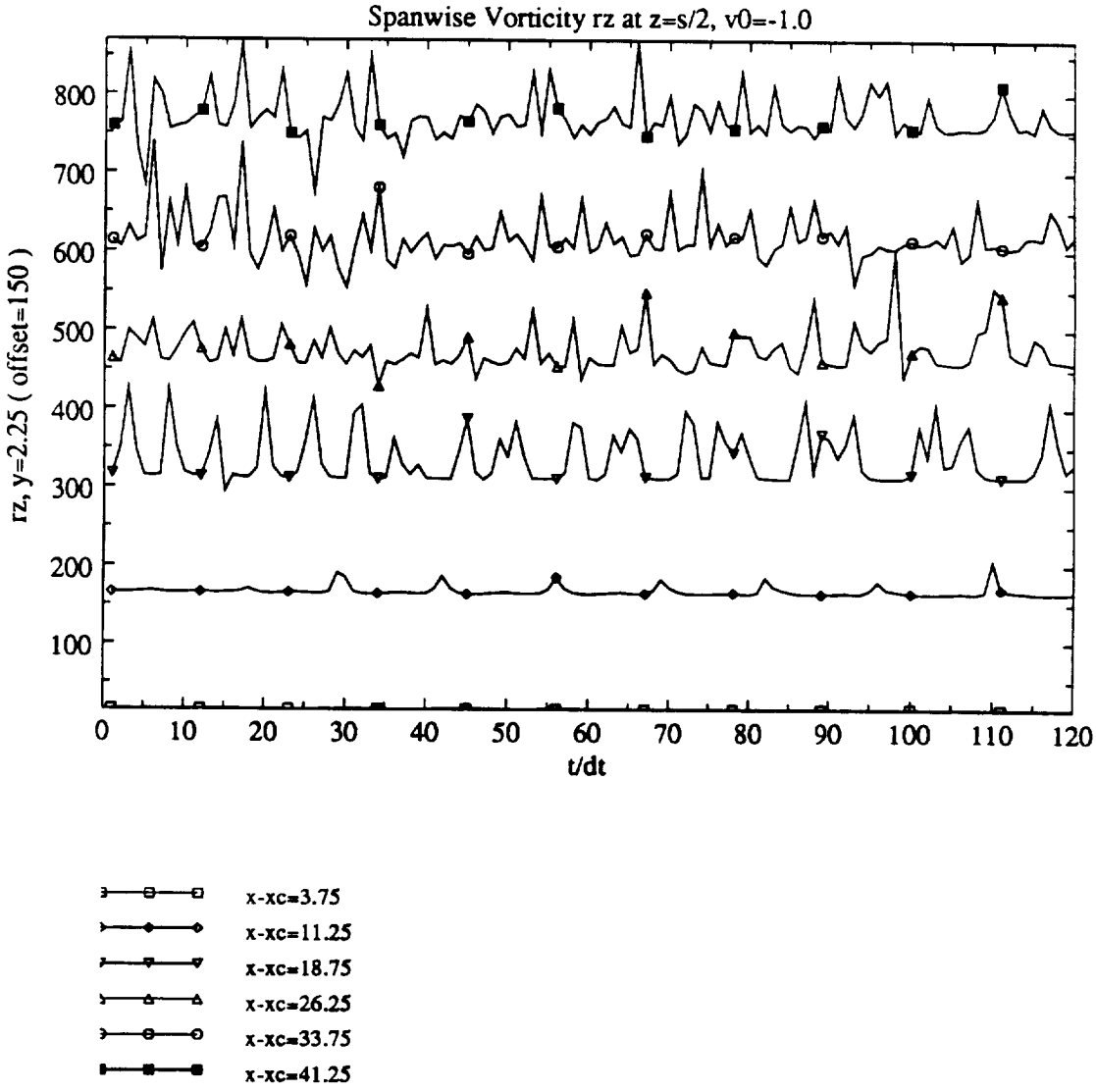

Figure 22: Case C3: ω_z plotted versus t, for several downstream locations x at constant $y = 2.25.$, $z = 1.003$

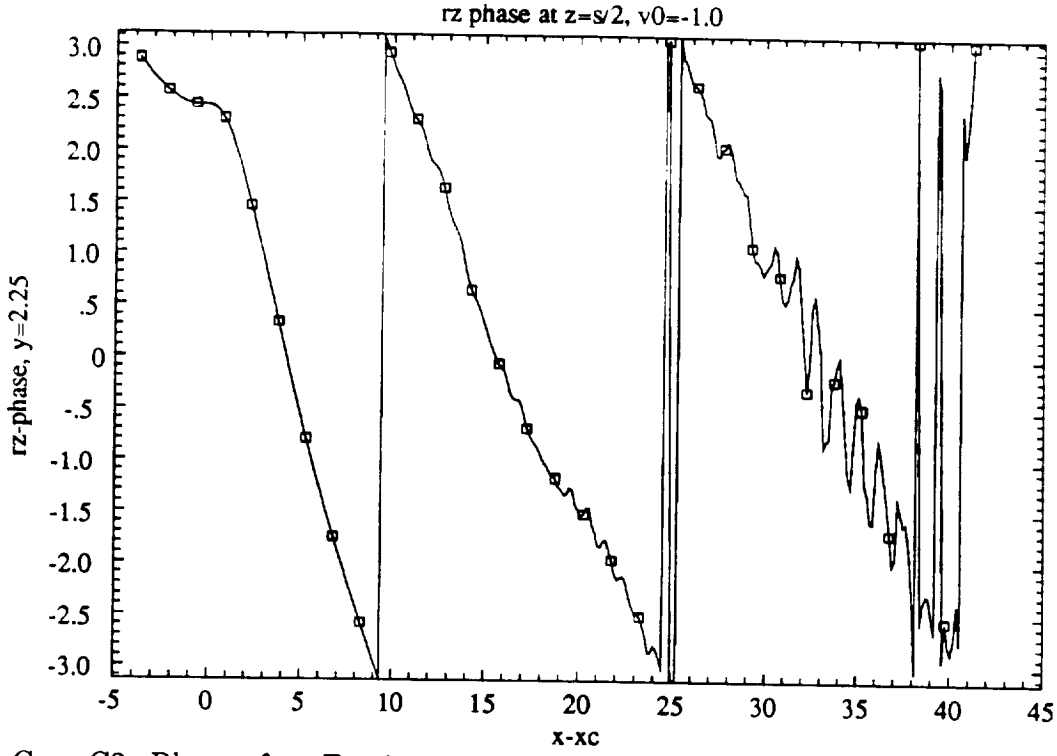

Figure 23: Case C3: Phase of ω_z Fourier component with frequency 735 Hz, plotted versus x at constant $y = 2.25, , z = 1.003$

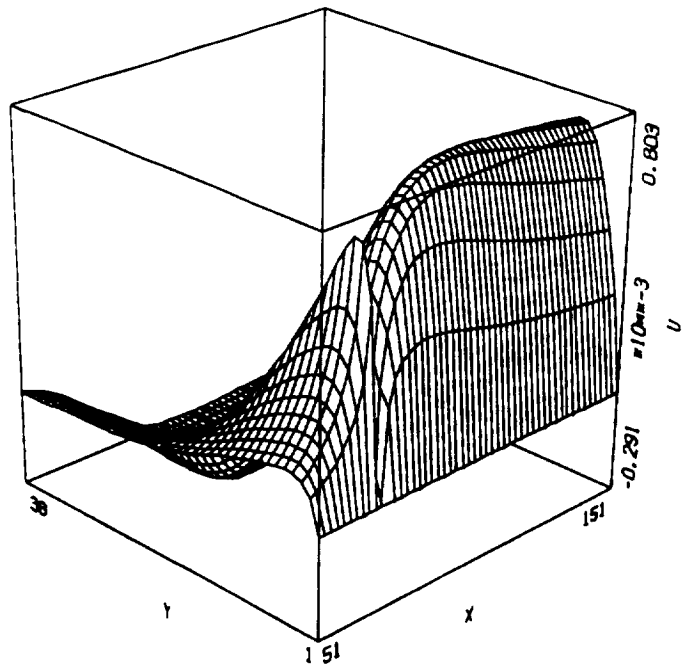

Figure 24: Carpet plot of mean 2-D streamwise velocity induced by small suction holes.

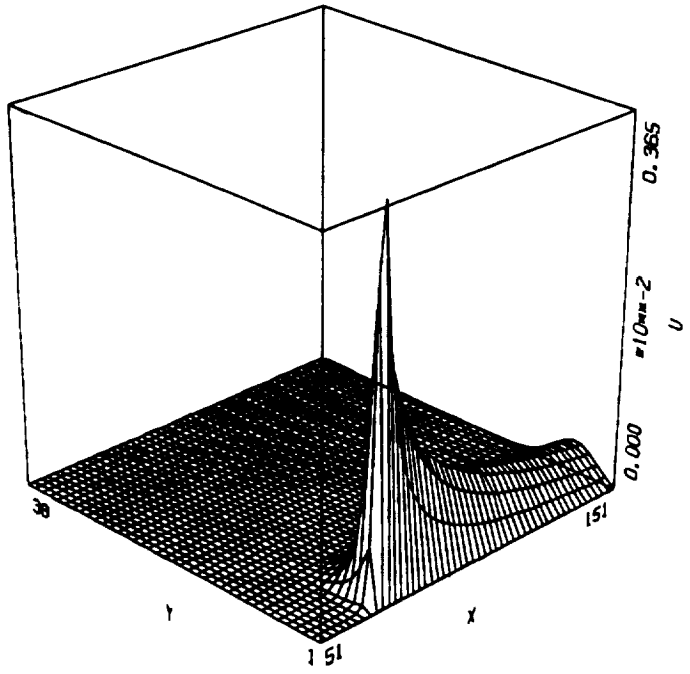

Figure 25: Carpet plot of first spanwise Fourier mode of streamwise velocity induced by small suction holes.

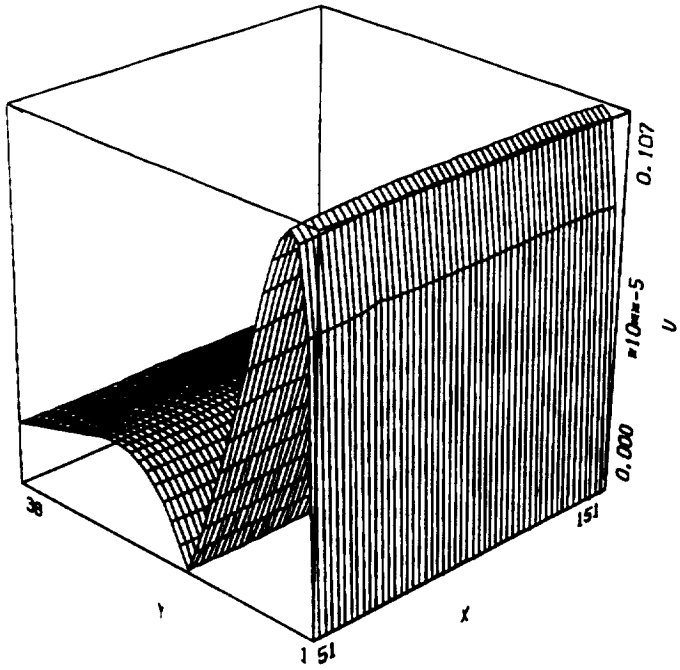

Figure 26: Carpet plot of u amplitude of 2-D TS-wave in boundary layer with small suction holes

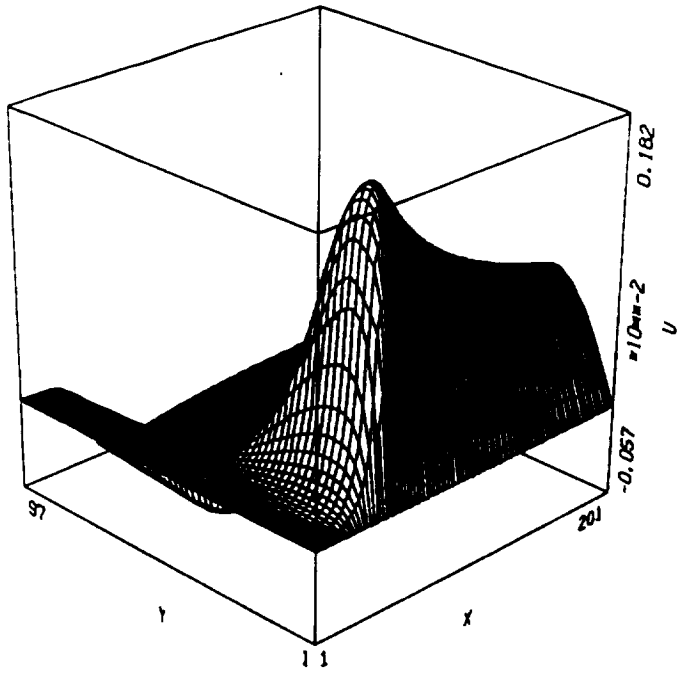

Figure 27: Carpet plot of mean 2-D streamwise velocity induced by large suction holes.

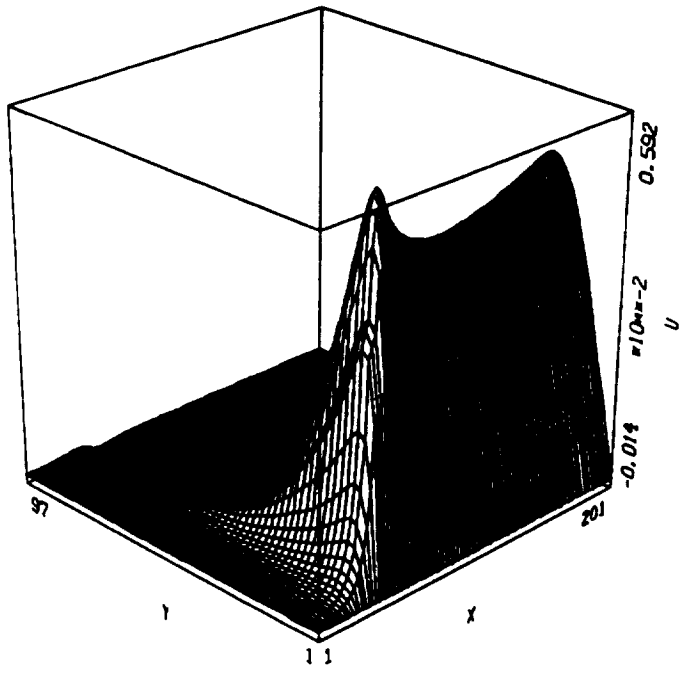

Figure 28: Carpet plot of first spanwise Fourier mode of streamwise velocity induced by large suction holes.